PHYSICAL REVIEW A **90**, 022707 (2014)

Radiative-electron-capture-to-continuum cusp in $U^{88+} + N_2$ collisions and the high-energy endpoint of electron-nucleus bremsstrahlung

P.-M. Hillenbrand,[1,2,*] S. Hagmann,[1,3,†] D. Atanasov,[1,4,5] D. Banaś,[6] K.-H. Blumenhagen,[1,7,8] C. Brandau,[2,9] W. Chen,[1]
E. De Filippo,[10] A. Gumberidze,[9,11] D. L. Guo,[12,13] D. H. Jakubassa-Amundsen,[14] O. Kovtun,[5] C. Kozhuharov,[1] M. Lestinsky,[1]
Yu. A. Litvinov,[1,4,5] A. Müller,[2] R. A. Müller,[7] H. Rothard,[15] S. Schippers,[2] M. S. Schöffler,[3] U. Spillmann,[1] A. Surzhykov,[7]
S. Trotsenko,[1,7] N. Winckler,[1] X. L. Yan,[4,12,13] V. A. Yerokhin,[16] X. L. Zhu,[12] and Th. Stöhlker[1,7,8]
[1]*GSI Helmholtzzentrum für Schwerionenforschung, D-64291 Darmstadt, Germany*
[2]*Institut für Atom- und Molekülphysik, Justus-Liebig-Universität Giessen, D-35392 Giessen, Germany*
[3]*Institut für Kernphysik, Goethe Universität Frankfurt, D-60438 Frankfurt am Main, Germany*
[4]*Max-Planck-Institut für Kernphysik, D-69117 Heidelberg, Germany*
[5]*Ruprecht-Karls Universität Heidelberg, D-69120 Heidelberg, Germany*
[6]*Institute of Physics, Jan Kochanowski University, PL-25-406 Kielce, Poland*
[7]*Helmholtz-Institut Jena, D-07743 Jena, Germany*
[8]*Institut für Optik und Quantenelektronik, Friedrich-Schiller-Universität Jena, D-07743 Jena, Germany*
[9]*ExtreMe Matter Institute EMMI and Research Division, GSI Helmholtzzentrum für Schwerionenforschung, D-64291 Darmstadt, Germany*
[10]*Istituto Nazionale di Fisica Nucleare Sezione di Catania, I-95123 Catania, Italy*
[11]*FIAS Frankfurt Institute for Advanced Studies, D-60438 Frankfurt am Main, Germany*
[12]*Institute of Modern Physics, Chinese Academy of Sciences, Lanzhou 730000, China*
[13]*University of Chinese Academy of Sciences, Beijing 100049, China*
[14]*Mathematisches Institut, Ludwig-Maximilians-Universität München, D-80333 München, Germany*
[15]*Centre de Recherche sur les Ions, les Matériaux et la Photonique, CIMAP-CIRIL-Ganil, F-14070 Caen, France*
[16]*Center for Advanced Studies, St. Petersburg State Polytechnical University, St. Petersburg 195251, Russia*

(Received 18 June 2014; published 11 August 2014)

The radiative electron capture of a target electron into the projectile continuum has been studied for the collision system $U^{88+} + N_2 \to U^{88+} + [N_2^+]^* + e^- + \gamma$ at 90 MeV/u. Using a magnetic electron spectrometer, the energy distribution of cusp electrons emitted under an angle of 0° with respect to the projectile beam and with a velocity close to the projectile velocity has been measured in coincidence with the emitted photons under various observation angles. The experimental results provide a stringent test for the corresponding process in inverse kinematics, namely, the theory of electron-nucleus bremsstrahlung at the high-energy endpoint. For comparison this process is calculated using fully relativistic Dirac wave functions and using semirelativistic Sommerfeld-Maue wave functions.

DOI: 10.1103/PhysRevA.90.022707 PACS number(s): 34.70.+e, 34.50.−s, 41.60.−m, 32.80.Fb

I. INTRODUCTION

Electron-nucleus bremsstrahlung is the process where an electron e^- with an initial kinetic energy E_i scatters off a nucleus Z and transfers part of its kinetic energy onto a photon γ, which is emitted. The underlying fundamental process is fully accessible if the scattering angle of the outgoing electron ϑ_f, the emission angle of the emitted photon ϑ_γ, and the energy of the outgoing electron E_f or of the emitted photon E_γ are observed:

$$e^-(E_i) + Z \to e^-(E_f,\vartheta_f) + Z + \gamma(E_\gamma,\vartheta_\gamma).$$

Since the kinetic energies of the outgoing particles obey energy conservation $E_i = E_f + E_\gamma$, the process has three independent observables. Consequently the highest sensitivity with respect to the fundamental process is reached by studying triple-differential cross sections $d^3\sigma/dE_f d\Omega_f d\Omega_\gamma$ as a function of the incident electron energy E_i and the target atomic number Z [1,2].

The high-energy endpoint—or, synonymously, the short-wavelength limit—of electron-nucleus bremsstrahlung is described by the highest energy transfer from the incoming electron to the emitted photon, i.e., $E_\gamma \approx E_i$ and $E_f \approx 0$. It can also be seen as a transition of a free electron from a high-energy continuum state E_i to a low-energy continuum state E_f in the Coulomb field of a nucleus Z while emitting a photon with energy E_γ. As such, it is one of a family of processes, which are closely related in their theoretical description: As shown by Fano *et al.* [3–7] and Pratt *et al.* [8–10], it is closely related to the transition of a free electron into a bound state of the nucleus under the emission of a photon, which is the process of radiative recombination. Radiative recombination itself is related to its time-reversed processes, namely, photoionization and electron-positron pair production, by the principle of detailed balance [5,11–13]. By comparing bremsstrahlung and radiative recombination it was shown theoretically that at the threshold dividing the two cases, i.e., the case of a finally free electron with negligibly low kinetic energy in the continuum $E_f \gtrsim 0$ and the case $E_f \lesssim 0$ resulting in a finally bound electron captured into a high-lying Rydberg state $n \to \infty$, both processes show comparable features in the differential cross sections and

---

[*] p.m.hillenbrand@gsi.de
[†] s.hagmann@gsi.de

thus show a smooth transition from one process to the other [5,9,14–16].

Analysis of the high-energy endpoint of electron-nucleus bremsstrahlung is a challenge both theoretically and experimentally. For an electron scattering off a bare nucleus, the theoretical description involves the transition between two continuum states in a Coulomb potential under the emission of a photon. For $E_f \to 0$ first-order theories such as the Born approximation fail to predict the correct behavior of the cross section, which is finite at the high-energy endpoint [1,2,17,18]. These theories are only valid for electrons with an incoming velocity β_i and an outgoing velocity β_f inelastically scattering off a nucleus of atomic number Z under the assumptions $\alpha Z/\beta_i \ll 1$ and $\alpha Z/\beta_f \ll 1$ with $\alpha \approx 1/137$. The latter assumption is, in particular, never true for the high-energy endpoint of bremsstrahlung with $\beta_f \to 0$. In this case advanced theories are required, and contributions of relativistic effects in the continuum wavefunctions become significant for heavier nuclei [3,19–21].

For the fundamental process of electron-nucleus bremsstrahlung the first kinematically complete experiments were pioneered by Nakel *et al.* [2,22]. In their setup electrons impinge on a very thin solid target foil and the energy and angular distribution of the scattered electrons are measured in coincidence with the emitted bremsstrahlung photon. However, the high-energy endpoint cannot be studied in this configuration, since an outgoing electron of $E_f \to 0$ is not detectable in this geometry. Furthermore, the cross section at the high-energy endpoint is influenced by the electron screening effects of the nucleus when working with atomic targets instead of bare ions, depending on the collision energy and the target species [14,16,19]. The screening effects lead to a cross section at the high-energy endpoint of the bremsstrahlung spectrum, which is reduced compared to the point-Coulomb results, thus preventing clean experimental conditions for electron-nucleus bremsstrahlung in pure Coulomb fields [14,19]. Recent measurements performed by Tashenov *et al.* [23,24] and by Märtin *et al.* [25] used an approach similar to that of Nakel *et al.* and studied the effects of a polarized incoming electron on the polarization of the emitted photon, but no coincidence with the scattered electron was applied.

The two described constraints of bremsstrahlung experiments in "classical" geometry are avoided when using inverse kinematics: Instead of scattering energetic electrons off an atomic target, bare heavy ions impinge on (quasi-free) electrons, i.e., an atomic target of comparably low atomic number. In this way, electron-screening effects in the electron-nucleus bremsstrahlung are eliminated. Inelastically scattered electrons with $E'_f \approx 0$ in the (primed) reference frame of the ionic projectile travel parallel to the projectile after the collision, with an electron velocity v_e that is similar to the projectile velocity $v_p \approx v_e$ in the (unprimed) laboratory frame. This process, closely related to the fundamental process of electron-nucleus bremsstrahlung, is termed radiative electron capture to continuum (RECC) or radiative ionization [26–28]. RECC in turn is closely related to radiative electron capture to bound states (REC) [29,30], analog to the described relationship between bremsstrahlung and radiative recombination. Measurements of triple-differential cross sections of RECC thus provide the most stringent tests for the theory of electron-nucleus bremsstrahlung and the wave functions of low-energy continuum states in the vicinity of the nucleus [3–10]. Since the cross section of RECC increases with the projectile charge approximately as $Z_p^{2.3}$, it can best be studied using highly charged heavy ions [31].

In the first attempts to study bremsstrahlung using inverse kinematics, just the emitted x rays were observed [32–36]. Only with the development of the first magnetic forward-angle electron spectrometer built in a heavy-ion storage ring did coincidence measurements of the emitted photon with the scattered electron become accessible for the high-energy endpoint of electron-nucleus bremsstrahlung [37]. This experiment gave a proof of principle, but significant discrepancies between experiment and theory were observed. In continuation of these studies we show here that we could improve both the experimental accuracy of the measurement and the theoretical description of the process.

In this paper we present a measurement of (relative) triple-differential cross sections $d^3\sigma/dE_f d\Omega_f d\Omega_\gamma$ at the high-energy endpoint, which we can consistently describe theoretically by calculations using fully relativistic Dirac theory [16,38]. We studied the system of beryllium-like U^{88+} projectiles colliding with a N_2 target at an ion energy of 90 MeV/u. The energy distributions of electrons emitted under $\vartheta_f = 0^\circ$ with respect to the projectile beam and a velocity v_e similar to the projectile velocity v_p (i.e., cusp electrons) were measured in coincidence with photons emitted under various observation angles. Thereby the angular distribution of bremsstrahlung photons from the high-energy endpoint in coincidence with the scattered electron could be determined, also illustrating the relationship to REC and its photon angular distribution. Furthermore, the results give a stringent test for the theoretical description of the radiative population of low-energy continuum states in strong Coulomb fields.

The paper is organized as follows: The experimental setup is described in Sec. II, the data analysis is explained in Sec. III, the concepts of the corresponding theories are reported in Sec. IV, and the results and discussion are presented in Sec. V.

II. EXPERIMENTAL SETUP

The experiment was performed at the heavy-ion accelerator facility of the GSI Helmholtzzentrum für Schwerionenforschung, where isotope-pure beams of (almost) all ion species up to bare uranium are routinely available. Details of the experimental setup with the electron spectrometer installed at the Experimental Storage Ring (ESR) are described in Ref. [39]. Briefly, a beam of U^{88+} was injected into the storage ring at 90.38 MeV/u, and after the application of electron cooling it intersected a supersonic gas-jet target of molecular nitrogen N_2. The number of injected ions, about 10^8, and gas-jet target area density of around 10^{12} particles/cm^2 led to an average luminosity of the order of $L \approx 100\ \mathrm{b}^{-1}\ \mathrm{s}^{-1}$. Due to the excellent vacuum in the ESR in the 10^{-11} mbar range, but large ionization and capture cross sections for U^{88+} at this energy, the beam lifetime was dominated by collisions in the target and not by residual gas background collisions, such that an injection was repeated every 60 s.

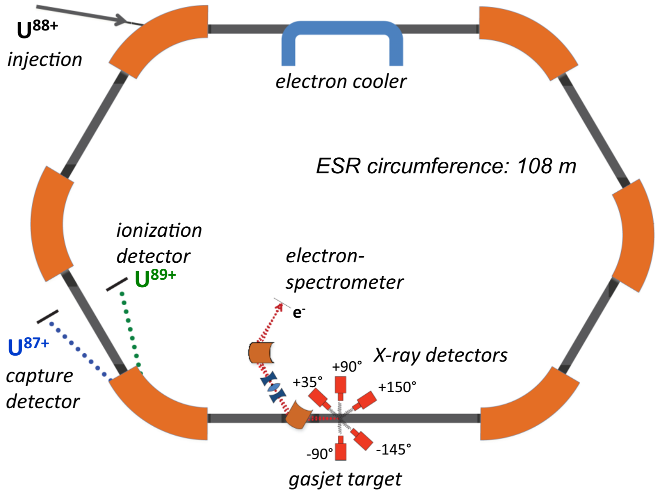

FIG. 1. (Color online) Layout of the experimental setup at the experimental storage ring ESR with the electron cooler, gas-jet target, electron spectrometer, x-ray detectors, and particle detectors for identification of projectile ionization and capture processes.

The unambiguous identification of the RECC process,

$$U^{88+} + N_2 \rightarrow U^{88+} + [N_2^+]^* + e^-(E_f,\vartheta_f) + \gamma(E_\gamma,\vartheta_\gamma),$$

requires coincident detection of the scattered electron e^- and the emitted photon γ. However, in the electron channel two additional competing processes under emission of a cusp electron, but without emission of a photon, occur for this collision system. An electron observed in the spectrometer may originate from RECC, or from nonradiative electron capture to continuum (ECC) [40],

$$U^{88+} + N_2 \rightarrow U^{88+} + [N_2^+]^* + e^-,$$

or from electron loss to continuum (ELC) [39],

$$U^{88+} + N_2 \rightarrow U^{89+} + [N_2]^* + e^-.$$

The usefulness and significance to the experiment of the latter two processes are explained later.

The electrons, originating from these three processes, are ejected from the interaction point at the gas-jet target into the forward direction with $v_e \approx v_p$. Their momentum is analyzed by the electron spectrometer (Fig. 1). The spectrometer consisted of two 60°-dipole magnets, each with a bending radius of 229 mm, and an iron-free quadrupole triplet in between the dipole magnets. The first 60° dipole, located 790 mm downstream from the gas-jet target, served both to magnetically separate the electrons from the ion beam and to analyze the momentum of the electrons. Its magnetic field was measured with a hall probe, whose values determined the electron momentum on a relative scale with a precision of better than 10^{-3}. The slight influence of the first spectrometer dipole magnet on the ion beam circulating in the storage ring was compensated by correction coils in the subsequent dipole magnet of the ring. With the combination of the first spectrometer dipole with the quadrupole triplet and the second dipole, an achromatic optics was realized in order to optimize the momentum as well as the angular acceptance for electrons being guided onto the position-sensitive electron detector. A combination of two microchannel plates in a chevron configuration and a hexagonal delay-line anode was used as the electron detector. It provided redundant reconstruction information on the electron impact position and decreased deadtime, compared to conventional rectangular delay-line anodes [41]. The information of the electron impact position ensured that the electrons guided through the spectrometer were always well focused on the detector. The traveling distance for the electrons from the interaction point to the electron detector was 4.2 m, the diameter of the aperture was everywhere along its path >90 mm, and the diameter of the active area of the detector was 75 mm. The geometry and optics of the spectrometer permitted detection of electrons emitted from the gas-jet target within the whole azimuthal emission angle of $\varphi_f = 0° - 360°$ for a polar angle $\vartheta_f = 0° - \vartheta_{\max} = 0° - 2.4°$ with respect to the projectile beam axis and a momentum spread of $\Delta p_e/p_e = 0.02$. The long distance between the interaction point and the electron detector additionally made sure that background from electrons scattered along the storage ring beam pipe was suppressed. However, time-of-flight effects were not considered since they could not be resolved experimentally.

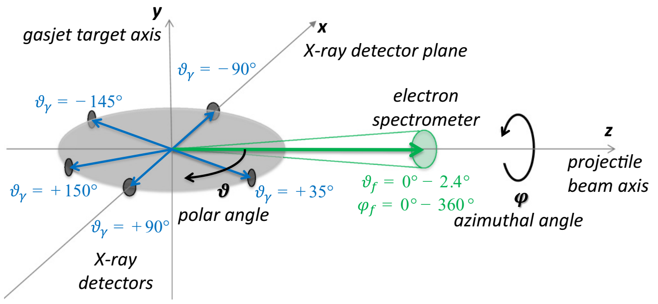

FIG. 2. (Color online) Geometry and coordinates in the laboratory system used throughout the paper: The horizontal projectile beam is intersected by the vertical gas-jet target; the angular acceptance of the electron spectrometer as well as the observation angles of the x-ray detectors in the horizontal xz-plane is shown.

Around the gas-jet target five high-purity germanium detectors were positioned at angles $\vartheta_\gamma = +35°, \pm 90°, -145°$, and $+150°$ with respect to the ion beam in the horizontal plane, in order to detect x rays emitted from the interaction point. Positive angles correspond to the right side, and negative angles to the left side, of the beam (Fig. 2).

For the purpose of normalization and diagnostics, two multiwire proportional chambers (MWPCs) were used to detect (with an efficiency of close to 100%) projectile ions which lost or captured an electron while traversing the gas-jet target or (at a small fraction) the residual gas (Fig. 1) [42]. These charge-changed projectile ions were magnetically separated from the primary projectile beam in the first ESR dipole magnet after the gas-jet target in order to hit one of the two MWPCs.

III. DATA ANALYSIS

Triple-differential cross sections $d^3\sigma/dE_f d\Omega_f d\Omega_\gamma$ as a function of the electron kinetic energy E_f under the electron emission angle of $\vartheta_f = 0^\circ$ for five photon emission angles ϑ_γ were determined from the number of electrons coincident with a photon $N_{e\wedge\gamma}$ as a function of the magnetic fields applied to the spectrometer:

$$\left.\frac{d^3\sigma^{\mathrm{RECC}}}{dE_f d\Omega_f d\Omega_\gamma}\right|_{\vartheta_f=0^\circ} = \frac{N_{e\wedge\gamma}}{L_{\mathrm{int}}}\frac{1}{\epsilon_e\Delta\Omega_e}\frac{1}{\epsilon_\gamma\Delta\Omega_\gamma} \times \frac{E_f+m_ec^2}{E_f^2+2E_fm_ec^2}\frac{1}{\Delta p_e/p_e}. \quad (1)$$

Here $\epsilon_e,\Delta\Omega_e$ and $\epsilon_\gamma,\Delta\Omega_\gamma$ are the detection efficiencies and the solid angle acceptances of the electron spectrometer and the x-ray detectors, respectively. The relative momentum acceptance of the spectrometer is given by $\Delta p_e/p_e$, which is a constant. The energy factor with the electron rest energy m_ec^2 includes both the conversion of momentum-differential to energy-differential cross sections dp_e/dE_f and the dispersion correction $1/p_e(\Delta p_e/p_e)$, i.e., the increasing absolute momentum acceptance with increasing momentum. The integrated luminosity L_{int} (in units of b^{-1}) was determined by integrating the product of the ion beam current $I_{\mathrm{ion}}(t)$ and target area density $n_{\mathrm{target}}(t)$ over the measurement time t, i.e.,

$$L_{\mathrm{int}} = \int \frac{I_{\mathrm{ion}}(t)n_{\mathrm{target}}(t)}{Z_pe}dt, \quad (2)$$

with $Z_pe = 88e$ being the projectile charge.

A relative systematic error of 20% for the evaluation of Eq. (1) was estimated due to uncertainties in the reproducibility and the energy dependence of the spectrometer efficiency ϵ_e while scanning its magnetic fields, the relative uncertainty in the determination of L_{int}, and the relative uncertainty in the determination of the x-ray detection efficiency and solid angle $\epsilon_\gamma\Delta\Omega_\gamma$. The latter was determined by comparing the x-ray spectra to L-REC cross sections known from experimentally confirmed theory [13,43]. In order to reduce uncertainties in the determination of L_{int} through Eq. (2), an independent normalization to the recombined U^{89+} ions detected in the corresponding MWPC was used. The relative systematic error was quadratically added to the statistical error, which was of comparable magnitude due to the small solid angles of the x-ray detectors of $\Delta\Omega_\gamma \approx (10^{-3}\text{–}10^{-4}) \times 4\pi$ and thus the low count rates.

Absolute cross sections were not derived directly due to the unknown electron detection efficiency ϵ_e. Instead, the cross sections extracted from the experiment by applying Eq. (1) were normalized to theory. For that a constant factor was fitted to the ratio of theoretical to experimental results by means of a weighted least-squares fit. Here one common normalization factor was determined for all five photon observation angles ϑ_γ. In this way the experimental data provide a test of theory not only for the electron energy distribution, but also for the corresponding photon angular distribution.

In a storage ring, the projectile velocity v_p of a cooled ion beam is given by the velocity of the electrons in the electron cooler [44]. Thus, for a given cooler voltage, the kinetic energy of the electrons in the cooler (corrected for space charge effects) is the same as that for cusp electrons, when they travel at a velocity equal to the projectile velocity $v_e = v_p$ after interaction with the gas-jet target. This electron collision energy is therefore denoted $E_0 = 49.58$ keV. From this energy the specific projectile kinetic energy of 90.38 MeV/u was deduced, as well as the projectile velocity in units of the speed of light, $\beta = v_p/c = 0.4112$ ($v_p = 56.33$ a.u.), and the corresponding Lorentz factor, $\gamma = 1 + E_0/(m_ec^2) = 1.097$, which are used throughout the paper.

The energy axis of the measured electron distributions was determined as follows: The magnetic field of the first momentum analyzing dipole of the spectrometer was measured on a relative scale using a hall probe to a precision on the level of 10^{-3}. This momentum axis was converted into an energy axis and was then calibrated using the ELC spectra measured simultaneously [39]. The ELC has a nearly symmetric cusp shape, such that its maximum is at E_0, independent of the precision to which E_0 is determined. Applying this *in situ* calibration method, the electron energy could be determined on an energy scale relative to E_0 with a precision of $\delta E_f/E_f = 0.01$. The possibility of observing the ELC channel simultaneously with the RECC channel as a diagnostic in our experimental setup is the reason that beryllium-like U^{88+} projectiles were used instead of bare U^{92+} ions.

The cross sections of nonradiative ECC and RECC both decrease with the collision velocity v_p^{-n}, but with different powers n. The projectile energy of about 90 MeV/u was chosen such that those two competing processes have similar cross sections for a nitrogen target, if all target electrons are taken into account [31]. This predicted "crossing velocity" was confirmed within our experiment, as described in a forthcoming paper on ECC [40].

IV. THEORY

A. Impulse approximation (IA)

The theoretical description of RECC in relativistic, strongly asymmetric collision systems ($Z_t \ll Z_p$) is conventionally based on the IA, a quantum mechanical three-body approach [26]. In a simplifying picture this theory can be viewed in terms of a convolution of the bremsstrahlung cross section with the momentum distribution of the initially bound electronic state. Thereby a given momentum component $\boldsymbol{q} = (\boldsymbol{q}_\perp, q_z)$ of the target bound-state wave function is Lorentz-boosted into $\boldsymbol{q}' = (\boldsymbol{q}'_\perp, q'_z)$ with $\boldsymbol{q}'_\perp = \boldsymbol{q}_\perp$ and $q'_z = \gamma(q_z - m_ev_p + E_Bv_p/c^2)$, where the z direction is chosen along $\boldsymbol{v}_p$, and the initial-state binding energy E_B is explicitly taken into account. Here and in the following, primed quantities refer to the projectile frame of reference, while unprimed quantities are defined in the target frame.

For the bremsstrahlung cross section the radiation matrix element is needed,

$$W_{\mathrm{rad}}(\boldsymbol{q}', m_s) = \langle \boldsymbol{p}'_f m_{s_f} | \boldsymbol{\alpha u}^*_\lambda\, e^{-i\boldsymbol{k}'\boldsymbol{r}} | \boldsymbol{q}' m_s \rangle, \quad (3)$$

which describes the transition of an electron from a scattering state $\psi_{\boldsymbol{q}'m_s}(\boldsymbol{r}) = \langle \boldsymbol{r} | \boldsymbol{q}'m_s \rangle$ to the final state $\psi_{\boldsymbol{p}'_f m_{s_f}}(\boldsymbol{r}) = \langle \boldsymbol{r} | \boldsymbol{p}'_f m_{s_f} \rangle$. These states are defined in the projectile frame of reference and are characterized by the respective asymptotic momenta of the initial target electron, $\boldsymbol{q}'$, of the final projectile continuum electron, $\boldsymbol{p}'_f \equiv \boldsymbol{p}'_e$, and by the spin projections, m_s and m_{s_f}. The electron scattering is accompanied by the emission of a photon with the wave vector $\boldsymbol{k}'$ and the polarization direction $\boldsymbol{u}_\lambda$ (relating to helicity λ).

The energy balance is given by

$$E'_f + E'_\gamma = E'_i - \gamma v_p q_z, \tag{4}$$

where $E'_\gamma = \hbar k' c$ is the photon energy and E'_i is the energy of the target electron. The relation of these energies to the experimental observables in the laboratory frame is given by the Lorentz transformation,

$$\begin{aligned} E'_i &= E_0 - \gamma E_B, \\ E'_f &= E_0 + \gamma E_f - \gamma v_p p_f \cos\vartheta_f, \\ E'_\gamma &= \gamma E_\gamma (1 - \beta \cos\vartheta_\gamma), \end{aligned} \tag{5}$$

where the electron collision energy $E_0 = (\gamma - 1) m_e c^2$ has been introduced and ϑ_f and ϑ_γ are, respectively, the emission angles of the electron and the photon.

The advantage of using semirelativistic Sommerfeld-Maue (SM) wave functions for the electronic states instead of fully relativistic Dirac functions is that the radiation matrix element of Eq. (3) can be calculated analytically [18,45]. As a consequence, the IA cross section can be evaluated without further approximations [26], which is not possible if Dirac functions, only accessible within a partial-wave representation, are used. The performance of the SM functions compared to the Dirac functions for a projectile as heavy as uranium was tested in a pilot calculation of the photon spectra from RECC [21]. In this calculation the additional integral over $\boldsymbol{q}'$ was eliminated by a transverse peaking approximation. While the results obtained from using Dirac functions were in good agreement with absolutely measured experimental data, the SM results revealed a global underestimate by a factor of 2. We attribute this behavior to the fact that for projectiles with a high nuclear charge Z_p and for slow scattered electrons, neither of the validity criteria for the SM functions ($E'_f \gg m_e c^2$ or $Z_p e^2/\hbar c \ll 1$) is satisfied.

B. Description of RECC in terms of bremsstrahlung

In the limit of vanishing target charge Z_t the triply differential RECC cross section, formulated within the IA, coincides in the vicinity of the cusp with the bremsstrahlung cross section evaluated in the projectile frame of reference and subsequently transformed into the target frame [46],

$$\begin{aligned} &\lim_{Z_t \to 0} \frac{d^3\sigma^{\text{IA}}}{dE_f d\Omega_f d\Omega_\gamma} \\ &\quad = \frac{1}{\gamma^2 (1 - \beta \cos\vartheta_\gamma)^2} \frac{\sin\vartheta'_f}{\sin\vartheta_f} \frac{d^3\sigma^{\text{brems}}}{dE'_f d\Omega'_f d\Omega'_\gamma}. \end{aligned} \tag{6}$$

The prefactor in Eq. (6) is the Lorentz transformation factor (see, e.g., [13,47]). An application of this prescription for targets with $Z_t \neq 0$ is more restrictive than the above-mentioned peaking approximation. It not only disregards the binding energy ($E_B = 0$), but also evaluates the radiation matrix element at $\boldsymbol{q} = \boldsymbol{0}$ (not only at $\boldsymbol{q}_\perp = \boldsymbol{0}$). This implies $\boldsymbol{q}' = (\boldsymbol{0}, -\gamma m_e v_p)$ in Eq. (3) as well as the conservation of the kinetic energies,

$$E'_f + E'_\gamma = E_0. \tag{7}$$

In short, the quasifree target electrons, characterized by their momentum distribution as described by the Compton profile $J(q_z)$, are replaced by Z_t free electrons when colliding with the projectile. We note that, instead of using $q'_z = -\gamma m_e v_p$ in Eq. (3), the standard prescription in bremsstrahlung theory, $q'_z = +\gamma m_e v_p$, has to go along with a simultaneous rotation of the projectile frame by 180° (or, equivalently, with reversal of the beam direction). This leads to the following modified relation between the projectile-frame angles ϑ'_f and ϑ'_γ and the observation angles ϑ_f and ϑ_γ,

$$\vartheta'_{f,\gamma} = \pi - \arctan\left[\frac{\sin\vartheta_{f,\gamma}}{\gamma(\cos\vartheta_{f,\gamma} - \beta/\beta_{f,\gamma})}\right], \tag{8}$$

where $\beta_f = p_f/m_e c$ and $\beta_\gamma = 1$.

Nevertheless, the free-electron approximation is justified since the experimental triply differential cross sections presented here imply an integration over the whole energy distribution of the photons or, equivalently, over the whole Compton profile, which is strongly peaked for loosely bound target electrons. Even for a nitrogen target, the deviations between the IA and the bremsstrahlung theory are at most 1%–2% in the cusp region (in the angular range $35^\circ \leqslant \vartheta_\gamma \leqslant 150^\circ$ covered by experiments), as estimated with the help of SM wave functions. One must, however, keep in mind that the correspondence between these two theories may be lost at extreme forward and backward photon angles (see the results for REC [13, Fig. 32]) or, in general, when experimental results are sensitive to the influence of the Compton profile.

C. Fully relativistic bremsstrahlung calculation

Having shown that the RECC cusp can basically be described in terms of the two-body bremsstrahlung in place of the IA, the theoretical analysis of the electron-photon coincidence measurements requires the knowledge of the triply differential bremsstrahlung cross section in the projectile frame. This cross section is usually evaluated within the framework of the first-order perturbation theory. Assuming that the incident electrons are unpolarized and neither the spin polarization of the scattered electrons nor the photon polarization is observed, it is given by [16,48–50]

$$\frac{d^3\sigma^{\text{brems}}}{dE'_f d\Omega'_f d\Omega'_\gamma} = \frac{e^2}{128\pi^2} \frac{k'}{p_i'^2} \sum_{\lambda m_{s_i} m_{s_f}} \left| W_{\text{rad}}(\boldsymbol{p}'_i, m_{s_i}) \right|^2, \tag{9}$$

where $\boldsymbol{p}'_i = \gamma m_e \boldsymbol{v}_p$ and $W_{\text{rad}}(\boldsymbol{p}'_i, m_{s_i})$ is defined in Eq. (3). The prefactor in Eq. (9) is written in relativistic units, accounting for the normalization of the electronic scattering states on an energy scale.

For further evaluation of the bremsstrahlung amplitude and the triply differential cross section of Eq. (9), knowledge is needed of the explicit form of the initial- and final-state electron wave functions. In this subsection we briefly recall the basics of using wave functions resulting from the Dirac theory. In this theory, the $\psi_{\boldsymbol{p}'_i m_{s_i}}(\boldsymbol{r})$ and $\psi_{\boldsymbol{p}'_f m_{s_f}}(\boldsymbol{r})$ are the solutions of the relativistic Dirac equation with some central potential $V(r)$. As usual in atomic collision studies, these *continuum* solutions are decomposed in terms of the partial (spherical) waves [13,49],

$$|\boldsymbol{p}'m_s\rangle = 4\pi \sum_{\kappa\mu} i^l e^{i\Delta_\kappa}\langle l m_l 1/2 m_s | j\mu\rangle Y^*_{lm_l}(\hat{\boldsymbol{p}}')|E'\kappa\mu\rangle, \tag{10}$$

where Δ_κ is the Coulomb phase shift which arises from the nuclear potential. These solutions for a continuum electron with momentum $\boldsymbol{p}'$ are used for both the initial electron $\boldsymbol{p}'_i$ and the final electron $\boldsymbol{p}'_f$. The summation in Eq. (10) runs over the relativistic quantum number $\kappa = \pm(j + 1/2)$ for $l = j \pm 1/2$, with l representing the parity of the partial component $|E'\kappa\mu\rangle$. Such a component is the Dirac eigenstate with the total energy $E' = \sqrt{p'^2c^2 + m_e^2c^4}$ and is represented by [13]

$$\langle \boldsymbol{r}|E'\kappa\mu\rangle = \begin{pmatrix} g_{E'\kappa}(r)\,\chi_{\kappa\mu}(\hat{\boldsymbol{r}}) \\ i f_{E'\kappa}(r)\,\chi_{-\kappa\mu}(\hat{\boldsymbol{r}}) \end{pmatrix}, \tag{11}$$

where $\chi_{\kappa\mu}$ denotes a standard Dirac spin-angular function. In order to determine the *radial* functions, $g_{E'\kappa}(r)$ and $f_{E'\kappa}(r)$, one has to decide about the potential $V(r)$ in which the electron moves. Since for the scattering of relatively fast electrons off highly charged heavy ions the *e-e* interactions play a minor role (cf. Ref. [16]), we consider here the case of a purely Coulombic potential for which the analytical expressions of $g_{E'\kappa}(r)$ and $f_{E'\kappa}(r)$ are well known from the literature [13].

By inserting the multipole expansion, Eq. (10), of the initial- and final-state electron wave functions into Eq. (3) and making use of the angular momentum algebra, one can finally calculate the triply differential bremsstrahlung cross section. For the details of these calculations we refer the reader to Refs. [16,38,50] and just mention here that their accuracy depends on the number of partial waves $|E'\kappa\mu\rangle$ used in Eq. (10) to represent the wave functions $\psi_{\boldsymbol{p}'_i m_{s_i}}(\boldsymbol{r})$ and $\psi_{\boldsymbol{p}'_f m_{s_f}}(\boldsymbol{r})$. In the calculations below, we employ all multipole components with $|\kappa_i| \leqslant 24$ and $|\kappa_f| \leqslant 8$ for the incident and scattered electron, respectively.

The triply differential cross section of Eq. (9), calculated within this partial-wave expansion of the Dirac wave functions, is displayed in Fig. 3(a) for the scattering of incident electrons with kinetic energy $E'_i = E_0 = 49.58$ keV off the bare ion with effective charge $Z = 88$. Here we present $d^3\sigma^{\text{brems}}/dE'_f d\Omega'_f d\Omega'_\gamma$ as a function of the electron emission angle ϑ'_f for four photon emission angles ϑ'_γ and for five kinetic energies E'_f of the outgoing electron.

The general behavior of the spectra can be understood as follows: At the high-energy endpoint of the electron-nucleus bremsstrahlung, the electron loses almost all its energy in the collision with the nucleus, such that $E'_f \approx 0$. This requires comparatively small impact parameters and large momentum transfers, which lead to backward scattering angles. Thus, at small E'_f, the cross section increases with ϑ'_f. As we move away from the high-energy endpoint and increase E'_f, the average impact parameter increases such that the maximum of the cross section eventually moves to smaller angles ϑ'_f.

For comparison, Fig. 3(b) shows the theoretical results for the angular distribution of the scattered electron within the bremsstrahlung prescription when SM wavefunctions are used instead. The same collision parameters are taken as in Fig. 3(a), with the restriction to $\vartheta_\gamma = 90°$. Comparison of the 90° calculations shown in Fig. 3(a) with those in Fig. 3(b) indicates not just a global difference in the absolute scale

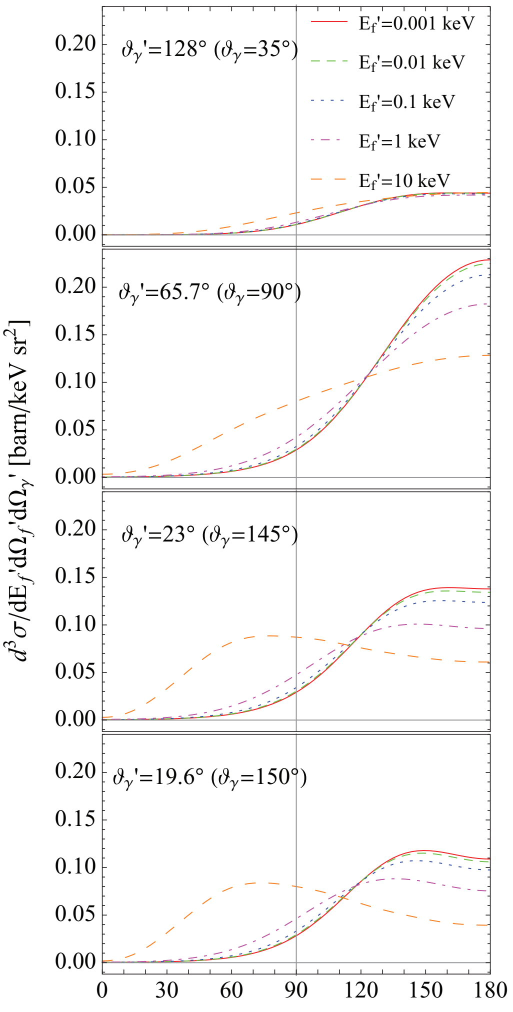

(a) Dirac theory

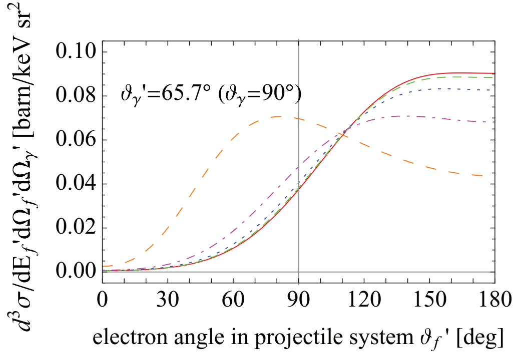

(b) Sommerfeld-Maue theory

FIG. 3. (Color online) Electron angular distribution in the projectile frame for different energies of the scattered electron E'_f and various photon observation angles ϑ_γ. Here the case is considered of an incoming electron of $E'_i = 49.58$ keV scattering off the projectile ion with $Z_p = 88$ while emitting a photon with energy $E'_\gamma = E'_i - E'_f$. Curves are as follows: $E'_f = 1$ eV (solid), $E'_f = 10$ eV (short-dashed), $E'_f = 100$ eV (dotted), $E'_f = 1$ keV (dot-dashed), and $E'_f = 10$ keV (long-dashed).

as in the case of the photon cross sections $d^2\sigma/dE_\gamma d\Omega_\gamma$ [21]. Instead, an increased intensity for $\vartheta'_f \lesssim 90^\circ$ and a lower intensity at the backward angles are found for the SM theory. Electrons scattered by 180° correspond to the smallest impact parameters and the largest momentum transfers. As argued in [21], the SM wave functions lack the relativistic contraction at small electron-nucleus distances and thus perform worst for that case. When transformed into the laboratory frame this leads to a smaller cusp width, as shown in Sec. V B.

D. Evaluation of the RECC cross section

When the theoretical triply differential cross sections are compared with the measured 0° electron spectra deduced from Eq. (1), the influence of the finite angular acceptance of the spectrometer has to be taken into consideration, which renders the RECC cusp finite. The spectrometer covers the laboratory-frame polar angles $0^\circ \leqslant \vartheta_f \leqslant \vartheta_{\max}$ (with $\vartheta_{\max} = 2.4^\circ$) and all azimuthal angles $0^\circ \leqslant \varphi_f \leqslant 360^\circ$ (Fig. 2). Therefore, theory has to be averaged over ϑ_f as well as over φ_f,

$$\left.\frac{d^3\sigma^{\mathrm{RECC}}}{dE_f d\Omega_f d\Omega_\gamma}\right|_{\vartheta_f=0^\circ} = \frac{1}{2\pi}\,\frac{1}{1-\cos\vartheta_{\max}}\,\frac{1}{\gamma^2(1-\beta\cos\vartheta_\gamma)^2} \times Z_t \int_0^{\vartheta_{\max}} \sin\vartheta'_f\, d\vartheta_f \int_0^{2\pi} d\varphi_f\, \frac{d^3\sigma^{\mathrm{brems}}}{dE'_f d\Omega'_f d\Omega'_\gamma}, \tag{12}$$

where Eq. (6) has been used. Furthermore, the momentum acceptance of the spectrometer, $\Delta p_e/p_e = 0.02$, is taken into account by folding the results of Eq. (12) with the corresponding energy acceptance $\Delta E_f/E_f = (\gamma+1)/\gamma \times \Delta p_e/p_e \approx 2 \times \Delta p_e/p_e$.

We note that the photon angle ϑ_γ is not affected by the averaging procedure in Eq. (12). Thus, for a given ϑ_γ, Eq. (12) has to be evaluated at ϑ'_γ as given by Eq. (8). Due to the Lorentz invariance of the azimuthal electron emission angle, one has $d\varphi_f = d\varphi'_f$, such that the φ_f average of the bremsstrahlung cross section can be performed in the projectile frame of reference. The remaining polar integration in Eq. (12) requires a two-dimensional interpolation of the projectile-frame (φ_f-averaged) bremsstrahlung cross section as a function of E'_f and ϑ'_f. To this end, the bremsstrahlung ϑ'_f distribution was calculated at five grid points, corresponding to the energies $E'_f = 1$ eV, 10 eV, 100 eV, 1 keV, and 10 keV, which cover the range 15 keV $\leqslant E_f \leqslant$ 100 keV for the chosen $\vartheta_{\max}$. Subsequently, a linear interpolation between the grid points was used. In the case of $E_f \leqslant E_0$ and $\vartheta_f \leqslant \vartheta_{\max}$, the angular region $0^\circ \leqslant \vartheta'_f \leqslant \vartheta'_{\max}$ contributes to the target-frame RECC cross section, while for $E_f \geqslant E_0$ it is $\vartheta'_{\max} \leqslant \vartheta'_f \leqslant 180^\circ$. In the limit $E_f \to E_0$ (i.e., $E'_f \to 0$) one has $\vartheta'_{\max} \approx 90^\circ$. This leads to the fact that we collect electrons with scattering angles extending from $\vartheta'_f = 0^\circ$ or $\vartheta'_f = 180^\circ$ almost up to $\vartheta'_f = 90^\circ$ for electron energies close to the cusp. On the other hand, when $E_f \ll E_0$ or $E_f \gg E_0$, only a small interval of projectile-frame scattering angles is sampled.

Eventually, the cross section evaluated through Eq. (12) includes, in our case of a N_2 target, the multiplication with the number of electrons in a nitrogen atom, $Z_t = 7$. We note that for the high collision energy considered here, the molecular character of the N_2 target can be neglected. Consequently, in the following all cross sections are given per target atom.

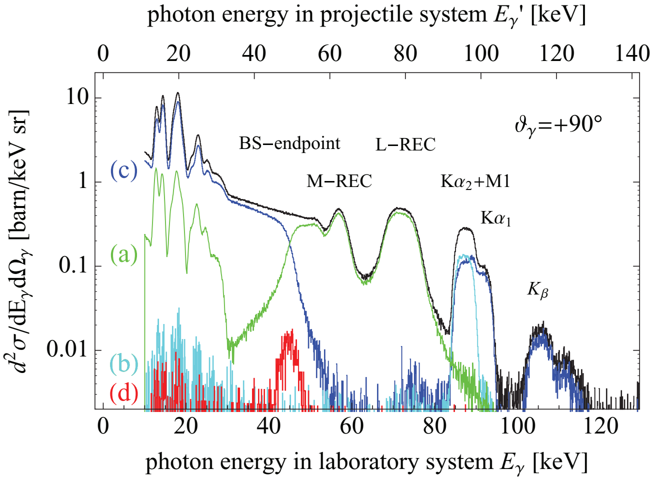

FIG. 4. (Color online) The x-ray energy spectrum observed under $\vartheta_\gamma = +90^\circ$ without any coincidence condition (black), (a) in coincidence with a down-charged projectile (green), (b) in coincidence with an up-charged projectile (cyan), (c) in anticoincidence with a charge-changed projectile (blue), and (d) in coincidence with an electron emitted under $\vartheta_f = 0^\circ$ (red).

V. RESULTS AND DISCUSSION

The aim of this work is to study electron-photon coincidences at the high-energy endpoint of electron-nucleus bremsstrahlung. Therefore it is important to understand the energy spectrum of both the electrons and the photons under different coincidence conditions, which provide controlled access to the physical processes that compete with the one studied here. The electron spectra of ELC and ECC, which were both studied simultaneously with the investigations presented here, are analyzed in Refs. [39,40], respectively. For the x-ray spectrum the competing processes are briefly summarized in Sec. V A, illustrating the clean experimental conditions for study of the high-energy endpoint. Section V B then discusses the main experimental results of the electron energy distribution, and these results are used in Sec. V C to determine the angular distribution of bremsstrahlung photons from the high-energy endpoint.

A. Photon energy distribution

Figure 4 shows the x-ray spectrum observed under $\vartheta_\gamma = +90^\circ$. By applying different well-defined coincidence conditions between the emitted x ray and a signal in one of the other detectors, various atomic processes occurring in collisions of beryllium-like U^{88+} ions with N_2 can be discerned.[1]

---

[1] A fraction of the U^{88+} projectiles produced in the stripper foil may be in the metastable $1s^2 2s 2p\ {}^3P_0$ state, which, according to Fig. 4.41 in Ref. [51], might not fully decay to the $1s^2 2s^2\ {}^1S_0$ ground state during the beam preparation time in the ESR of about 8 s, before the measurement phase begins.

(a) The coincidence of the x-ray photon with the down-charged projectile (green data in Fig. 4) shows events where an electron from the target was radiatively captured into a bound projectile state of the L shell, the M shell, or any higher shell (L-REC, M-REC) [29,30,52]. In addition, capture processes with a subsequent emission of a characteristic photon during relaxation are seen, such as

$$\mathrm{U}^{88+}(1s^2 2s^2) + \mathrm{N}_2 \rightarrow \mathrm{U}^{87+}(1s^2 2s^2 nl) + [\mathrm{N}_2^+]^* + \gamma.$$

After efficiency correction and normalization of the x-ray spectrum to the L-REC cross sections known from experimentally confirmed theory [13,43,52], the absolute scale of the double-differential cross sections $d^2\sigma/dE_\gamma d\Omega_\gamma$ in Fig. 4 was determined. Moreover, the product of detection efficiency and solid angle acceptance $\epsilon_\gamma \Delta\Omega_\gamma$ was determined for all x-ray detectors and used for the evaluation of Eq. (1).

(b) By applying a coincidence condition between the emitted x ray and the up-charged projectile (cyan in Fig. 4), processes of selective K-shell ionization of the projectile with a subsequent emission of a photon become visible, including two-electron one-photon decay [53],

$$\begin{aligned}\mathrm{U}^{88+}(1s^2 2s^2) + \mathrm{N}_2 &\rightarrow \mathrm{U}^{89+}(1s2ll') + [\mathrm{N}_2]^* + e^- \\ &\rightarrow \mathrm{U}^{89+}(1s^2 2l) + [\mathrm{N}_2]^* + e^- + \gamma.\end{aligned}$$

(c) If only those x-ray events are selected where the projectile has neither captured nor lost one electron (measured via anticoincidence with close to 100% detection efficiency of all charge-changed projectiles [42]), events associated with pure excitation and subsequent de-excitation become visible (blue in Fig. 4):

$$\mathrm{U}^{88+} + \mathrm{N}_2 \rightarrow [\mathrm{U}^{88+}]^* + [\mathrm{N}_2]^* \rightarrow \mathrm{U}^{88+} + [\mathrm{N}_2]^* + \gamma.$$

Furthermore, the photons from the bremsstrahlung can be seen, with the finite cross section at the endpoint. As can be seen, the high-energy slope is stretched by the target Compton profile [cf. Eq. (4)], the Doppler broadening due to the finite observation angle, and the energy resolution of the x-ray detector used.

(d) In the coincidence of x-ray photons with the electrons observed in the electron spectrometer (red in Fig. 4), only photons from the high-energy endpoint of the bremsstrahlung are observed (neglecting background events). In comparison with the other coincidences it is obvious that these events correspond directly to the radiative electron capture of a target electron into the low-energy projectile continuum RECC, right at the transition from the capture into bound states to the capture into unbound states of the projectile:

$$\mathrm{U}^{88+} + \mathrm{N}_2 \rightarrow \mathrm{U}^{88+} + [\mathrm{N}_2^+]^* + e^- + \gamma.$$

The energy distribution of E_γ is given by Eqs. (4) and (5), its peak position being in accordance with energy conservation during electron-nucleus bremsstrahlung. As shown in Fig. 5, the maximum of the *electron* distribution of the RECC is slightly higher than the cusp energy of E_0. To get a maximum yield of coincident events for the spectrum in Fig. 4, the electron spectrometer was set to an energy of $E_f = 53.23$ keV, corresponding in the projectile frame to $E_f' = 62$ eV and a centroid photon energy in the laboratory frame of $E_\gamma = 45.13$ keV. The width of the line is given by the momentum acceptance of the electron spectrometer and is then broadened by the target Compton profile and by the other effects listed in item (c) above.

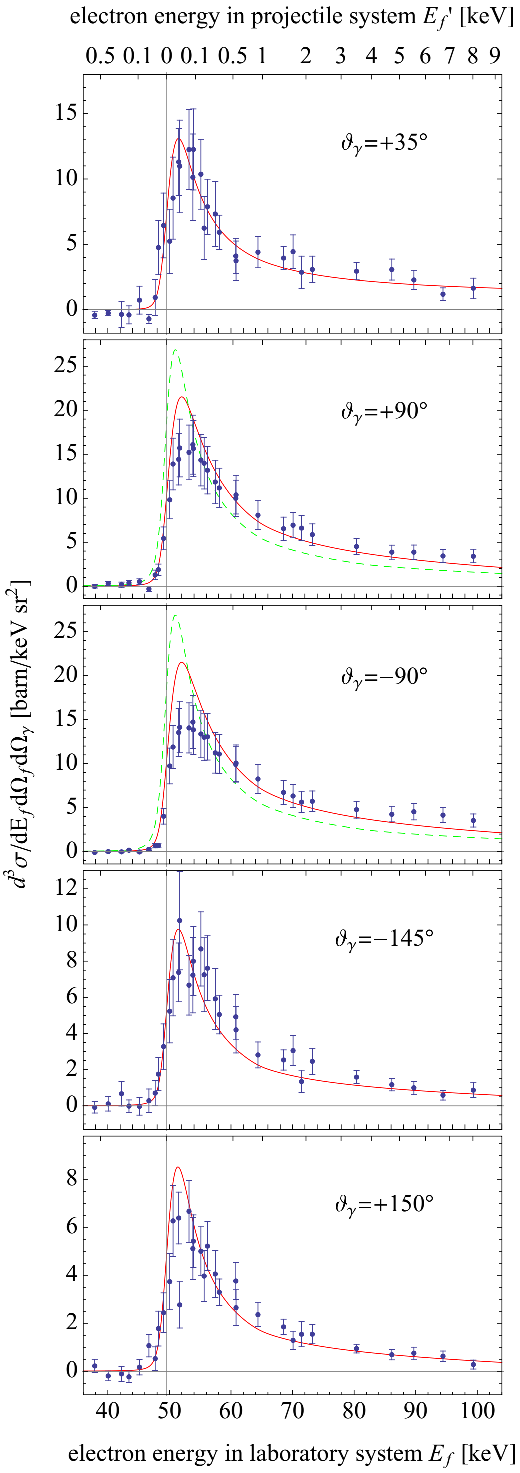

FIG. 5. (Color online) Experimental and theoretical electron energy distributions at the high-energy endpoint of bremsstrahlung observed under $\vartheta_f = 0^\circ$ for five different photon emission angles ϑ_γ: Dirac theory (solid red line), Sommerfeld-Maue theory multiplied by 2 (dashed green line) for $\vartheta_\gamma = \pm 90^\circ$. The experimental results (symbols) are normalized to Dirac theory, the same scaling factor is applied to for all five photon angles ϑ_γ.

B. Electron energy distribution

In Fig. 5 the measured triple-differential cross sections $d^3\sigma/dE_f d\Omega_f d\Omega_\gamma$ as a function of the electron kinetic energy E_f are shown, averaged over the electron emission angle $\vartheta_f = 0°\text{–}2.4°$ for five photon emission angles: $\vartheta_\gamma = +35°, \pm 90°, -145°$, and $+150°$. The spectra show the energy distribution of electrons being radiatively captured from the target into the projectile continuum. In inverse kinematics these electrons are interpreted as having undergone deeply inelastic scattering off the projectile while emitting a bremsstrahlung photon. Electrons having the cusp energy of $E_f \approx E_0$ (indicated by the vertical line) in the laboratory and $E'_f \approx 0$ in the projectile frame correspond to photons from the high-energy endpoint of the bremsstrahlung. The energy of the bremsstrahlung photon E_γ is determined by the continuum electron kinetic energy in the projectile frame E'_f through $E'_\gamma = E_0 - E'_f$ and Eqs. (5). This behavior given by energy conservation was experimentally confirmed within the uncertainty of the data for all electron energies and all photon observation angles.

As can be seen from the calculations shown in Figs. 3(a) and 3(b), in electron-nucleus bremsstrahlung electrons with a low projectile-frame energy $E'_f \leqslant 1$ keV are scattered predominantly into the backward direction $\vartheta'_f > 90°$. The transformation described in Sec. IV D with the integration over $\vartheta'_f = 0° - \vartheta'_{\max}$ in the case of $E_f < E_0$ and over $\vartheta'_f = \vartheta'_{\max} - 180°$ in the case of $E_f > E_0$ then leads to the fact that the spectrum is dominated by electrons with $E_f > E_0$, while contributions of $E_f < E_0$ are negligible. The theoretical triple-differential cross sections presented in Sec. IV are also shown in Fig. 5. The experimental electron energy distributions were normalized to the result of fully relativistic bremsstrahlung theory as described in Sec. III by applying one common scaling factor for all five photon emission angles ϑ_γ.

For $\vartheta_\gamma = \pm 90°$ a comparison of the theoretical results using Dirac wave functions with the calculations using SM wave functions shows, besides a factor of ≈2 on the absolute scale, a significantly narrower cusp width for the SM theory. As shown in Fig. 3, this is attributed to an underestimation of the cross section for backward-scattered electrons in the projectile frame $\vartheta'_f \approx 180°$ in SM theory. Even though the relative experimental results cannot contradict the validity of SM theory on an absolute scale, the broader cusp shape resulting from the application of Dirac theory is clearly confirmed by the experiment. Thus, the significant discrepancy between experiment and theory shown by Nofal *et al.* for the same collision system [37] could be resolved by improving the theoretical description of the process as well as by improving the experimental accuracy of the measurement. Due to a proper calibration of the electron energy axis using the ELC, the results reveal that the maximum of the distribution is well above the cusp energy E_0, in contrast to the data shown in Ref. [37].

Some remaining small discrepancies can be seen in the spectra in Fig. 5 for $\vartheta_\gamma \pm 90°$, where experimental cross sections in the maximum of the cusp are significantly lower than the results of Dirac theory. From the experimental viewpoint, this discrepancy might be attributed to an underestimation of the electron maximum angular acceptance $\vartheta_{\max}$, the value of which was cross-checked with the ELC spectrum studied simultaneously within the same experiment [39]. However, this parameter is crucial in the evaluation of Eq. (12) and has a strong influence on the cusp shape. For the electron spectrometer used in this experiment, $\vartheta_{\max}$ is in principle limited by geometrical considerations, but some uncertainties in the exact transmission efficiency as a function of $\vartheta_f = 0° - \vartheta_{\max}$ remain. From the theoretical viewpoint, uncertainties may arise in the choice of the upper limits for κ_i and κ_f in the summation of the relativistic partial waves, Eq. (10). However, these values were carefully checked in order to reach sufficient convergence.

The experimental data shown in Fig. 5 are characterized by a strongly asymmetric cusp shape, which is dominated by electrons with $E_f > E_0$. In both the experimental and the theoretical results, the cusp shape of the scattered electron appears to depend only weakly on the emission angle of the bremsstrahlung photon ϑ_γ. A detailed analysis shows that the cusp shape for $\vartheta_\gamma = 90°$ is slightly broader compared to the other photon angles ϑ_γ studied here. Moreover, for large photon emission angles $\vartheta_\gamma = 145°$ and $150°$ the cross section decreases more rapidly at high energies, $E_f > 60$ keV, than for smaller angles ϑ_γ. These details can all be traced back to the corresponding behavior in the projectile frame given in Fig. 3(a): e.g., the cross section at $\vartheta'_f = 180°$ in the projectile frame as a function of E'_f determines the decreasing cross section in the laboratory frame for high electron energies E_f, and the cross section integrated from $\vartheta'_f \gtrsim 90°$ up to $\vartheta'_f = 180°$ determines the high-energy slope of the cusp [cf. Eq. (12)].

The asymmetry of the cusp shape for the RECC was predicted by theory to increase significantly with the projectile charge Z_p and to decrease with the projectile velocity v_p approximately as $Z_p/\gamma v_p$ [26]. Thus, the asymmetry is expected to be particularly pronounced and unprecedentedly visible for the U^{88+} projectiles used in this experiment. Furthermore, the asymmetry of the RECC cusp shape for this collision system was predicted to be opposite to the cusp shape of nonradiative ECC, which is dominated by electrons with $E_f < E_0$ [26]. This behavior could be experimentally confirmed by the electron energy spectrum for RECC presented in this paper, in comparison with the spectrum of the ECC measured in parallel within this experiment. Details will be given in a forthcoming publication [40]. The opposite asymmetry of the two competing processes can best be explained and visualized by taking into account also the Compton profile of the target: While for the radiative process energy and momentum conservation is facilitated through the emission of a photon [cf. Eq. (4)], this degree of freedom is not available for the nonradiative process ($E'_\gamma = 0$). While for RECC (integrated over the photon energy) an electron of any momentum component of the Compton profile can contribute, ECC requires a large initial momentum of the target electron, of the order of $q_z \approx \gamma m_e v_p$, thus only outer wings of the Compton profile $J(q_z)$ contribute. RECC involves a deeply inelastic scattering of a quasifree electron close to the nucleus with the emission of a photon. In the projectile frame, the incoming electron is guided around the projectile and is scattered under backward angles $\vartheta'_f \approx 180°$ (cf. Fig. 3), which corresponds to $E_f > E_0$ in the laboratory frame. In contrast, in ECC

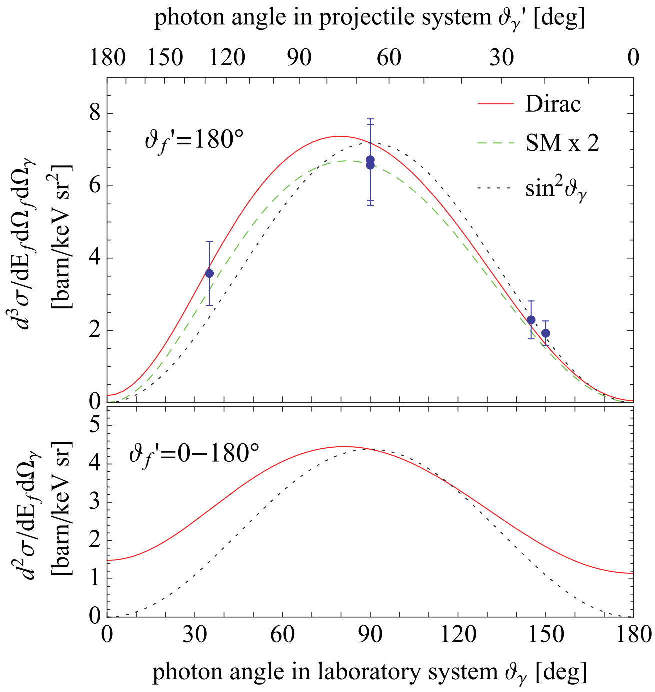

FIG. 6. (Color online) Photon angular distribution at the high-energy endpoint of electron-nucleus bremsstrahlung, emitted for an electron energy of $E_f' = 1$ keV. Experimental results (symbols) in comparison with Dirac theory (solid red line), Sommerfeld-Maue theory multiplied by 2 (dashed green line), and a $\sin^2\vartheta_\gamma$-like dipole radiation pattern (dotted black line). Top, triple differential cross sections for an electron emission angle of $\vartheta_f' = 180°$; bottom, double differential cross sections integrated over all electron emission angles.

the electron from the outer wing of the Compton profile is attracted by the projectile but scatters quasielastically under small scattering angles $\vartheta_f' \approx 0°$. In the laboratory frame the electron is dragged behind the projectile without being able to pass it, thus it is observed only with $E_f < E_0$ [28].

C. Photon angular distribution

The angular distribution of photons at the high-energy endpoint is shown in Fig. 6 (top). Experimental values for the triple-differential cross sections $d^3\sigma/dE_f d\Omega_f d\Omega_\gamma$ as a function of the photon emission angle ϑ_γ for an outgoing electron of $E_f' = 1$ keV corresponding to a laboratory electron energy of $E_f = 65.1$ keV, i.e., on the high-energy slope of the RECC cusp, have been taken from the data set shown in Fig. 5. This electron energy was chosen since for electron energies closer to the cusp $E_f \approx E_0$, the transverse electron energy acceptance $E_{f\perp} = E_f \cdot \sin^2\vartheta_{\max} \approx 0.1$ keV is no longer negligible. Since the transverse component cannot be resolved experimentally, this limits the electron energy resolution in the projectile system. Furthermore, at the chosen electron energy the electron angular acceptance in the projectile system of $\vartheta_f' = 180°–164°$ permits us to deduce the theoretical photon angular distribution from the triple-differential cross sections for $\vartheta_f' = 180°$, without having to average over the electron angular acceptance of ϑ_f' (cf. Fig. 3). The relative experimental cross sections were normalized to Dirac theory, similar to the spectra shown in Fig. 5. The relative systematic errors for the photon angular distribution are not influenced by uncertainties in the electron detection efficiency, but only by uncertainties in the relative photon detection efficiency and solid angle $\epsilon_\gamma \Delta\Omega_\gamma$, which were assumed to be 10% and were quadratically added to the statistical error.

The theoretical photon angular distributions shown in Fig. 6 were calculated by the Dirac and SM theory as described in Sec. IV and are compared to a classical dipole radiation $\sim\sin^2\vartheta_\gamma$. In Fig. 6 (top) triple-differential cross sections are given, whereas in Fig. 6 (bottom) double-differential cross sections are shown, integrated over all emission angles of the outgoing electron ϑ_f' and φ_f'. The triple-differential cross sections calculated with SM wave functions are—almost independently of ϑ_γ—a global factor of 2 lower than the corresponding cross sections using Dirac wave functions (cf. Sec. IV A), a result to which the relative experimental cross sections are insensitive.

The experimental photon angular distribution deviates noticeably from a pure $\sin^2\vartheta_\gamma$ distribution. However, the experimental data do not contain sufficient statistical significance to preclude one theoretical calculation over the other. For the double-differential cross sections no experimental values could be deduced due to the restricted angular acceptance of the spectrometer, $\Delta\Omega_e \approx \pi\vartheta_{\max}^2$. The comparison shows the benefit of studying triple-differential cross sections instead of (integrated) double-differential cross sections, as discussed in the following.

According to classical electrodynamics the angular distribution of the bremsstrahlung photon is proportional to $\sin^2\vartheta_\gamma$ in the rest frame of the incoming electron, where ϑ_γ is the photon emission angle with respect to the acceleration felt by the electron [2,54]. Since in this experiment the rest frame of the incoming electron is identical to the laboratory frame, and the acceleration felt by the electron is parallel to the projectile beam for electrons being scattered under $\vartheta_f' = 180°$, a $\sin^2\vartheta_\gamma$-like dipole radiation is expected to be observed in the laboratory frame according to classical considerations. It can thus also be understood that the double-differential cross section, integrated over all electron emission angles ϑ_f', has a clear deviation from a $\sin^2\vartheta_\gamma$ distribution around $\vartheta_\gamma \approx 0°$ and $\vartheta_\gamma \approx 180°$ (Fig. 6, bottom): Although the emission of the electron close to $\vartheta_f' = 180°$ is dominant, as shown in Fig. 3, the integration over all emission angles ϑ_f' corresponding to an integration over all possible directions of acceleration felt by the electron leads to this deviation.

The photon angular distribution of RECC can be directly compared to that of REC. The photon angular distribution for an electron recombining radiatively into a bound final *s* state is also similar to a $\sin^2\vartheta_\gamma$ distribution in the laboratory frame and has been explained for REC to result from a mutual cancellation of two effects [55], namely, the retardation of the photon wave function in the projectile frame and the Lorentz transformation from the projectile to the laboratory frame: When the full photon wave $\sim e^{-i\mathbf{k}'\cdot\mathbf{r}}$ in Eq. (3) is taken into account instead of the dipole approximation ($e^{-i\mathbf{k}'\cdot\mathbf{r}} = 1$), retardation effects become visible and lead to a forward-backward asymmetry of the photon angular distribution in the projectile frame. Only after application of the Lorentz transformation is the resulting photon distribution symmetric and $\sin^2\vartheta_\gamma$-like in the laboratory frame [55]. Deviations from the $\sin^2\vartheta_\gamma$ distribution and the resulting forward-backward asymmetry in the laboratory frame were attributed to contributions of relativistic effects [56]. More precisely, a finite cross section in the photon angular distribution at $\vartheta_\gamma = 0^\circ$ for recombination into s states could only be explained by a spin-flip process [29,30]. However, these arguments are not applicable to recombination into bound states with orbital angular momentum $l \geqslant 1$, where finite cross sections at $\vartheta_\gamma = 0^\circ$ and $\vartheta_\gamma = 180^\circ$ are possible due to angular momentum conservation even in the nonrelativistic approximation [57].

Since RECC is theoretically treated in the same framework as REC, the same arguments apply [16]. The angular distribution of photons emitted during recombination into a bound state with principal quantum number n, summed over all possible substates ljm, is characterized by a slight asymmetry, with a preference towards forward angles in the laboratory system, $\vartheta_\gamma < 90^\circ$ [57]. A similar behavior can be seen in the photon distribution determined for the RECC in Fig. 6. To reach sufficient convergence in the theoretical triple-differential cross sections using partial-wave analysis of the Dirac wave functions, partial waves up to $l = 8$ were included for $E'_f \leqslant 1$ keV, which indicate the contributions of continuum wave functions far beyond s waves.

VI. SUMMARY AND OUTLOOK

The energy distribution of electrons originating from RECC has been measured, corresponding to the high-energy endpoint of bremsstrahlung in inverse kinematics. While previous measurements of bremsstrahlung have examined mostly double-differential cross sections or the polarization of the bremsstrahlung photon, the results presented here provide experimental tests for triple-differential cross sections in the vicinity of the high-energy endpoint of bremsstrahlung, which are only accessible in the presented configuration of inverse kinematics.

The experimental data have been compared with the bremsstrahlung theory developed by Surzhykov and Yerokhin using fully relativistic Dirac wave functions [16,38] as well as with the RECC theory developed by Jakubassa-Amundsen applying SM wave functions [26–28]. The results imply a measurement of the probability of populating a low-energy projectile-ion continuum state with a given energy E'_f under emission of a photon as a function of E'_f. The relative triple-differential cross sections have been shown to be consistently described by the theory of electron-nucleus bremsstrahlung applying Dirac theory. Discrepancies between experiment and theory observed in the previous experiment [37] could be resolved by improving both the experimental accuracy and the theoretical description of the process. In addition, the measurement of the photon angular distribution for RECC illustrates the inherent relation to REC.

Going beyond triple-differential cross sections of the elementary process of electron-nucleus bremsstrahlung, additional observables can be studied when taking into account the degree of polarization of the incoming electron, the outgoing electron, and/or the emitted photon. Also, investigations of in-plane $(\varphi_e - \varphi_\gamma = 0)$ and out-of-planes $(\varphi_e - \varphi_\gamma > 0)$ electron distribution appear highly desirable. Theoretical studies of such polarization-dependent triple-differential cross sections applying Dirac theory are currently being performed [50]. Testing their validity will again require new experimental developments.

The possibilities of performing electron (and positron) spectroscopy at heavy-ion storage rings will be greatly enhanced at the new Facility for Antiproton and Ion Research (FAIR). Compared to the projectile energies available at the ESR, the energy range of highly charged ions available will be extended towards lower energies at CRYRING@ESR [58] and towards higher energies at HESR [59]. For the investigation of RECC highly charged heavy ions at low energies are advantageous since both the cross section and the asymmetry of the RECC cusp increase with decreasing projectile energy [26,31]. Using a hydrogen target, the projectile energy at which RECC and ECC are comparably large was estimated to be around 11 MeV/u independent of the projectile charge [31]; this energy region will be accessible at CRYRING@ESR. While RECC deals with the population of positive continuum states, the corresponding excitation of electrons out of negative continuum states will be observable at the high-energy storage-ring HESR in the creation of electron-positron pairs [60–62].

ACKNOWLEDGMENTS

We would like to express our thanks to the members of the ESR team for their collaboration. P.-M.H. gratefully acknowledges the support from HIC-for-FAIR through HGS-HIRe. This work was supported by Helmholtz-CAS Joint Research Group HCJRG-108, by Helmholtz Alliance Program of the Helmholtz Association Contract No. HA216/EMMI (Extremes of Density and Temperature: Cosmic Matter in the Laboratory), and by BMBF Contracts No. 06GI911I and No. 05P12R6FAN.

---

[1] H. Bethe and W. Heitler, Proc. R. Soc. Lond. A **146**, 83 (1934).
[2] E. Haug and W. Nakel, *The Elementary Process of Bremsstrahlung* (World Scientific, Singapore, 2004).
[3] U. Fano, H. W. Koch, and J. W. Motz, Phys. Rev. **112**, 1679 (1958).
[4] U. Fano, K. McVoy, and J. Albers, Phys. Rev. **116**, 1147 (1959).
[5] U. Fano, Phys. Rev. **116**, 1156 (1959).
[6] U. Fano, K. McVoy, and J. Albers, Phys. Rev. **116**, 1159 (1959).
[7] K. W. McVoy and U. Fano, Phys. Rev. **116**, 1168 (1959).
[8] R. Pratt, Phys. Rev. **120**, 1717 (1960).
[9] R. H. Pratt and H. K. Tseng, Phys. Rev. A **11**, 1797 (1975).
[10] R. Jabbur and R. Pratt, Phys. Rev. **129**, 184 (1963).
[11] K. McVoy and F. Dyson, Phys. Rev. **106**, 1360 (1957).
[12] R. Pratt, Phys. Rev. **117**, 1017 (1960).

[13] J. Eichler and T. Stöhlker, Phys. Rep. **439**, 1 (2007).
[14] C. M. Lee, L. Kissel, R. H. Pratt, and H. K. Tseng, Phys. Rev. A **13**, 1714 (1976).
[15] I. J. Feng, I. B. Goldberg, Y. S. Kim, and R. H. Pratt, Phys. Rev. A **28**, 609 (1983).
[16] V. A. Yerokhin and A. Surzhykov, Phys. Rev. A **82**, 062702 (2010).
[17] G. Elwert, Ann. Phys. **426**, 178 (1939).
[18] G. Elwert and E. Haug, Phys. Rev. **183**, 90 (1969).
[19] H. K. Tseng and R. H. Pratt, Phys. Rev. A **3**, 100 (1971).
[20] H. K. Tseng and R. H. Pratt, Phys. Rev. A **7**, 1502 (1973).
[21] D. H. Jakubassa-Amundsen and V. A. Yerokhin, Eur. Phys. J. D **67**, 4 (2013).
[22] W. Nakel, Z. Phys. **214**, 168 (1968).
[23] S. Tashenov, T. Bäck, R. Barday, B. Cederwall, J. Enders, A. Khaplanov, Y. Poltoratska, K.-U. Schässburger, and A. Surzhykov, Phys. Rev. Lett. **107**, 173201 (2011).
[24] S. Tashenov, T. Bäck, R. Barday, B. Cederwall, J. Enders, A. Khaplanov, Y. Fritzsche, K.-U. Schässburger, A. Surzhykov, V. A. Yerokhin, and D. Jakubassa-Amundsen, Phys. Rev. A **87**, 022707 (2013).
[25] R. Märtin, G. Weber, R. Barday, Y. Fritzsche, U. Spillmann, W. Chen, R. D. DuBois, J. Enders, M. Hegewald, S. Hess, A. Surzhykov, D. B. Thorn, S. Trotsenko, M. Wagner, D. F. A. Winters, V. A. Yerokhin, and T. Stöhlker, Phys. Rev. Lett. **108**, 264801 (2012).
[26] D. H. Jakubassa-Amundsen, J. Phys. B **36**, 1971 (2003).
[27] D. H. Jakubassa-Amundsen, J. Phys. B **40**, 2719 (2007).
[28] D. H. Jakubassa-Amundsen, in *Radiation Physics Research Progress* (Novapublishers, New York, 2008), pp. 155–191.
[29] T. Stöhlker, T. Ludziejewski, F. Bosch, R. W. Dunford, C. Kozhuharov, P. H. Mokler, H. F. Beyer, O. Brinzanescu, B. Franzke, J. Eichler, A. Griegal, S. Hagmann, A. Ichihara, A. Krämer, J. Lekki, D. Liesen, F. Nolden, H. Reich, P. Rymuza, Z. Stachura, M. Steck, P. Swiat, and A. Warczak, Phys. Rev. Lett. **82**, 3232 (1999).
[30] T. Stöhlker, X. Ma, T. Ludziejewski, H. F. Beyer, F. Bosch, O. Brinzanescu, R. W. Dunford, J. Eichler, S. Hagmann, A. Ichihara, C. Kozhuharov, A. Krämer, D. Liesen, P. H. Mokler, Z. Stachura, P. Swiat, and A. Warczak, Phys. Rev. Lett. **86**, 983 (2001).
[31] D. H. Jakubassa-Amundsen, Eur. Phys. J. D **41**, 267 (2007).
[32] A. Yamadera, K. Ishii, K. Sera, M. Sebata, and S. Morita, Phys. Rev. A **23**, 24 (1981).
[33] H. Tawara, T. Azuma, T. Ito, K. Komaki, Y. Yamazaki, T. Matsuo, T. Tonuma, K. Shima, A. Kitagawa, and E. Takada, Phys. Rev. A **55**, 808 (1997).
[34] R. Anholt, C. Stoller, J. D. Molitoris, D. W. Spooner, E. Morenzoni, S. A. Andriamonje, W. E. Meyerhof, H. Bowman, J.-S. Xu, Z.-Z. Xu, J. O. Rasmussen, and D. H. H. Hoffmann, Phys. Rev. A **33**, 2270 (1986).
[35] T. Ludziejewski, T. Stöhlker, S. Keller, H. Beyer, F. Bosch, O. Brinzanescu, R. W. Dunford, B. Franzke, C. Kozhuharov, D. Liesen, A. E. Livingston, G. Menzel, J. Meier, P. H. Mokler, H. Reich, P. Rymuza, Z. Stachura, M. Steck, L. Stenner, P. Swiat, and A. Warczak, J. Phys. B **31**, 2601 (1998).
[36] G. Weber, Ph.D. thesis, University of Heidelberg (2010).
[37] M. Nofal, S. Hagmann, T. Stöhlker, D. H. Jakubassa-Amundsen, C. Kozhuharov, X. Wang, A. Gumberidze, U. Spillmann, R. Reuschl, S. Hess, S. Trotsenko, D. Banas, F. Bosch, D. Liesen, R. Moshammer, J. Ullrich, R. Dörner, M. Steck, F. Nolden, P. Beller, H. Rothard, K. Beckert, and B. Franczak, Phys. Rev. Lett. **99**, 163201 (2007).
[38] V. A. Yerokhin, A. Surzhykov, R. Märtin, S. Tashenov, and G. Weber, Phys. Rev. A **86**, 032708 (2012).
[39] P.-M. Hillenbrand *et al.* (unpublished).
[40] P.-M. Hillenbrand *et al.* (unpublished).
[41] O. Jagutzki, A. Cerezo, A. Czasch, R. Dörner, M. Hattas, M. Huang, V. Mergel, U. Spillmann, K. Ullmann-Pfleger, T. Weber, H. Schmidt-Böcking, and G. Smith, IEEE Trans. Nucl. Sci. **49**, 2477 (2002).
[42] O. Klepper and C. Kozhuharov, Nucl. Instrum. Methods B **204**, 553 (2003).
[43] O. Matula (private communication, 2012).
[44] H. Poth, Nature **345**, 399 (1990).
[45] A. Nordsieck, Phys. Rev. **93**, 785 (1954).
[46] D. H. Jakubassa-Amundsen, R. A. Müller, A. Surzhykov, and V. A. Yerokhin [Eur. Phys. J. D (to be published)].
[47] A. Voitkiv and J. Ullrich, *Relativistic Collisions of Structured Atomic Particles*, Springer Series on Atomic, Optical, and Plasma Physics No. 49 (Springer, Berlin, 2008).
[48] H. K. Tseng, J. Phys. B **30**, L317 (1997).
[49] H. K. Tseng, J. Phys. B **35**, 1129 (2002).
[50] R. A. Müller, V. A. Yerokhin, and A. Surzhykov [Phys. Rev. A (to be published)].
[51] D. Bernhardt, Ph.D. thesis, Justus-Liebig-Universität, Giessen (2012).
[52] T. Stöhlker, H. Geissel, H. Irnich, T. Kandler, C. Kozhuharov, P. H. Mokler, G. Münzenberg, F. Nickel, C. Scheidenberger, T. Suzuki, M. Kucharski, A. Warczak, P. Rymuza, Z. Stachura, A. Kriessbach, D. Dauvergne, B. Dunford, J. Eichler, A. Ichihara, and T. Shirai, Phys. Rev. Lett. **73**, 3520 (1994).
[53] S. Trotsenko, T. Stöhlker, D. Banas, C. Z. Dong, S. Fritzsche, A. Gumberidze, S. Hagmann, S. Hess, P. Indelicato, C. Kozhuharov, M. Nofal, R. Reuschl, J. Rzadkiewicz, U. Spillmann, A. Surzhykov, M. Trassinelli, and G. Weber, J. Phys.: Conf. Ser. **58**, 141 (2007).
[54] J. D. Jackson, *Classical Electrodynamics*, 3rd ed. (Wiley, New York, 1999).
[55] E. Spindler, H. D. Betz, and F. Bell, Phys. Rev. Lett. **42**, 832 (1979).
[56] A. Ichihara, T. Shirai, and J. Eichler, Phys. Rev. A **49**, 1875 (1994).
[57] J. Eichler, A. Ichihara, and T. Shirai, Phys. Rev. A **51**, 3027 (1995).
[58] P.-M. Hillenbrand, S. Hagmann, T. Stöhlker, Y. Litvinov, C. Kozhuharov, U. Spillmann, V. Shabaev, K. Stiebing, M. Lestinsky, A. Surzhykov, A. Voitkiv, B. Franzke, D. Fischer, C. Brandau, S. Schippers, A. Müller, D. Schneider, D. Jakubassa, A. Artiomov, E. DeFilippo, X. Ma, R. Dörner, and H. Rothard, Phys. Scripta **T156**, 014087 (2013).
[59] S. Hagmann, T. Stöhlker, Y. Litvinov, C. Kozhuharov, P.-M. Hillenbrand, U. Spillmann, V. Shabaev, K. Stiebing, M. Lestinsky, A. Surzhykov, A. Voitkiv, B. Franzke, D. Fischer, D. Schneider, D. Jakubassa, A. Artiomov, E. DeFilippo, X. Ma, R. Dörner, and H. Rothard, Phys. Scripta **T156**, 014086 (2013).

[60] A. N. Artemyev, T. Beier, J. Eichler, A. E. Klasnikov, C. Kozhuharov, V. M. Shabaev, T. Stöhlker, and V. A. Yerokhin, Phys. Rev. A **67**, 052711 (2003).

[61] A. N. Artemyev, V. M. Shabaev, T. Stöhlker, and A. S. Surzhykov, Phys. Rev. A **79**, 032713 (2009).

[62] T. Stöhlker, Y. A. Litvinov, V. Bagnoud, U. Bechstedt, C. Dimopoulou, A. Dolinskii, C. Geppert, S. Hagmann, T. Katayama, T. Kühl, R. Maier, W. Nörtershäuser, D. Prasuhn, R. Schuch, M. Steck, and H. Stockhorst, Phys. Scripta **T156**, 014085 (2013).